EUROPEAN JOURNAL OF COMPUTATIONAL MECHANICS
2018, VOL. 27, NO. 3, 204–228
https://doi.org/10.1080/17797179.2018.1485340

Taylor & Francis
Taylor & Francis Group

On modelling three-dimensional elastodynamic wave propagation with boundary spectral element method

Fangxin Zou and M H Aliabadi

Department of Aeronautics, Imperial College London, South Kensington Campus, London, UK

ABSTRACT

In this paper, a boundary spectral element method (BSEM) for solving the problem of three-dimensional wave propagation is introduced. In the new formulation, elastodynamics of structures is computed by the Laplace transformed boundary element method (BEM), and boundaries of structures are discretised into high-order isoparametric spectral elements. Three types of spectral elements – Lobatto, Gauss–Legendre and Chebyshev elements – have been implemented. With a significantly higher computational efficiency than the conventional BEM, the BSEM provides a competitive alternative for modelling high-frequency wave propagation in engineering applications.

ARTICLE HISTORY
Received 21 August 2017
Accepted 27 February 2018

KEYWORDS
Boundary element method; boundary integral equation; wave propagation; spectral element method; Lobatto element; Gauss–Legendre element; Chebyshev element

Introduction

Wave propagation in three-dimensional structures has been studied extensively. While analytic solutions (Eringen & Suhubi, 2013) are widely available for structures with simple geometries, numerical tools, such as the finite element method (FEM) (Zienkiewicz & Taylor, 2000) and the boundary element method (BEM) (Aliabadi, 2002), were developed many decades ago for modelling structures that involve complexities. Comparing to the FEM, the BEM only requires the discretisation of the boundaries of structures, and consequently all variables in the BEM are computed on the boundaries only. This leads to a considerable reduction in the complexity of meshing, especially for structures with irregular shapes, and also smaller systems of equations and a lower demand on computational resources. Lately, advanced algorithms for representing and solving the systems of equations in the BEM have further improved the computational efficiency of the method (Benedetti, Aliabadi, & Davi, 2008; Benedetti & Aliabadi, 2010; Mallardo & Aliabadi, 2012; Shen & Liu, 2007).

CONTACT Fangxin Zou frank.zou@polyu.edu.hk
Present address for Fangxin Zou is Interdisciplinary Division of Aeronautical and Aviation Engineering, The Hong Kong Polytechnic University, Hong Kong.

In recent years, structural health monitoring (SHM) has become a favourable approach for ensuring the safety of engineering structures in service. Most damage detection techniques make use of *smart structures* in which high-frequency ultrasonic waves are excited and propagate (Giurgiutiu, 2005; Ihn & Chang, 2004; Sharif-Khodaei & Aliabadi, 2014). Also, impact events can be effectively monitored through analysing the high-frequency elastic waves that are induced by the impacts (Haywood, Coverley, Staszewski, & Worden, 2004; Mallardo, Aliabadi, & Khodaei, 2013; Mallardo, Sharif-Khodaei, & Aliabadi, 2016; Worden & Staszewski, 2000). So far, the FEM has been the most commonly used tool for simulating wave-based SHM applications. The spectral element method (SEM), which was first introduced by Patera (1984) for modelling fluid flows, has also gained much interest in this area (Ha & Chang, 2010; Kim, Ha, & Chang, 2008; Peng, Meng, & Li, 2009; Żak, 2009). The SEM has been particularly favoured for solving high-frequency wave propagation in large-scale structures. In addition to SHM, it has also been well exploited in seismology (Komatitsch, Barnes, & Tromp, 2000; Komatitsch & Tromp, 1999, 2002; Komatitsch & Vilotte, 1998). Comparing to low-order finite elements, spectral elements exhibit much faster mesh convergence. Also, they are numerically more accurate and stable than conventional high-order elements with equally spaced nodes (Gottlieb & Orszag, 1983).

On the other hand, Zou et al. (Zou & Aliabadi, 2015; Zou, Benedetti, & Aliabadi, 2014) developed the first boundary element formulations which are capable of modelling the full functionality of piezoelectric *smart structures* in ultrasonic wave-based damage detection applications. Although their methods require less computational resources and demonstrate a higher numerical stability than the conventional FEM, they still struggle in resolving high-frequency wave propagation in large-scale structures. In the field of BEM, the first applications of spectral elements appeared in 1990s and are in the scope of fluid mechanics (Muldowney & Higdon, 1995; Occhialini, Muldowney, & Higdon, 1992). To the best of the authors' knowledge, these elements have not been implemented in the BEM for modelling elastodynamic wave propagation.

In this paper, the first boundary spectral element method (BSEM) for solving the problem of wave propagation in three-dimensional structures is presented. The Laplace transformed three-dimensional BEM is employed to compute the elastodynamic responses of structures, and high-order spectral elements are implemented to carry out boundary discretisation. Parametric studies and numerical experiments have been conducted to assess the performances of the various types of spectral elements and to validate the new formulation. By achieving a high computational efficiency and owing to some of attractive features of the BEM, the BSEM will

become a competitive numerical tool for modelling high-frequency wave propagation in modern engineering applications.

Boundary spectral element method

Boundary integral equation (BIE) in Laplace domain

In the absence of body forces, the Navier–Cauchy equation, which governs the dynamics of an isotropic elastic body, is given by (Aliabadi, 2002, p. 196)

$$c_2^2 u_{i,kk}(X,t) + \left(c_1^2 - c_2^2\right) u_{k,ki}(X,t) = \ddot{u}_i(X,t), [X \in \Omega] \tag{1}$$

where c_1 and c_2 are the velocities of the longitudinal and the shear waves, and $\boldsymbol{u}$ is the displacement at a point $\boldsymbol{X}$ in the domain Ω of the body. The Laplace transform of Equation (1) can be written as (Aliabadi, 2002, p. 201)

$$c_2^2 u_{i,kk}(\boldsymbol{X},s) + \left(c_1^2 - c_2^2\right) u_{k,ki}(\boldsymbol{X},s) = s^2 u_i(\boldsymbol{X},s), \ [\boldsymbol{X} \in \Omega] \tag{2}$$

By using Somigliana identity, the displacement at a point $\boldsymbol{X}'$ in the domain of the body can be related to the displacements and the tractions along the boundary Γ such that (Aliabadi, 2002, p. 201)

$$\begin{aligned} u_i(\boldsymbol{X}',s) = &\int_\Gamma U_{ij}(\boldsymbol{X}',\boldsymbol{x},s) t_j(\boldsymbol{x},s) d\Gamma \\ &- \int_\Gamma T_{ij}(\boldsymbol{X}',\boldsymbol{x},s) u_j(\boldsymbol{x},s) d\Gamma, \ [\boldsymbol{X}' \in \Omega, \boldsymbol{x} \in \Gamma] \end{aligned} \tag{3}$$

where $\boldsymbol{X}'$ and $\boldsymbol{x}$ are known as the source and the field point, and U_{ij} and T_{ij} are the Laplace transformed fundamental solutions of elastodynamic displacement and traction (see Appendix A) (Wen, Aliabadi, & Rooke, 1998). By moving the source point to the boundary (i.e. imposing the limit $\boldsymbol{X}' \to \boldsymbol{x}'$), the displacement BIE can be obtained as (Aliabadi, 2002, p. 202)

$$c_{ij}(\boldsymbol{x}') u_i(\boldsymbol{x}',s) + \int_\Gamma T_{ij}(\boldsymbol{x}',\boldsymbol{x},s) u_j(\boldsymbol{x},s) d\Gamma = \int_\Gamma U_{ij}(\boldsymbol{x}',\boldsymbol{x},s) t_j(\boldsymbol{x},s) d\Gamma, \ [\boldsymbol{x}' \in \Gamma] \tag{4}$$

where the value of c_{ij} depends on the location of the source point.

Boundary discretisation

In order to evaluate the displacement BIE, the boundary of the body is discretised into elements. Isoparametric spectral elements, which employ high-order interpolating polynomials as their shape functions, are used for both geometry representation and the approximation of boundary displacements and tractions.

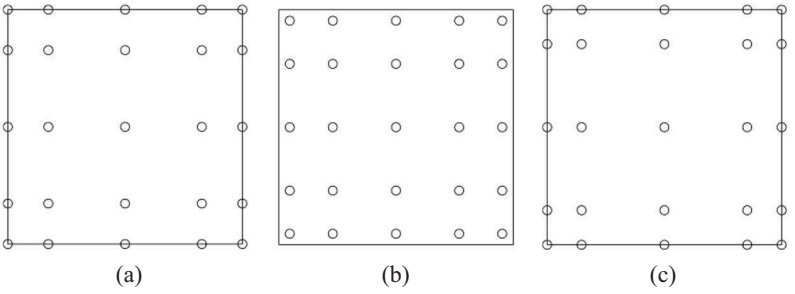

Figure 1. 25-Node configuration of (a) Lobatto, (b) Gauss–Legendre and (c) Chebyshev elements.

Three types of spectral elements (examples of which are shown in Figure 1) have been implemented in this work. These elements, which differ in node locations and shape functions, can be categorised into Lagrange polynomial-based and Chebyshev polynomial-based approximations. The general expressions for the interpolation of the geometry and the displacement and the traction field within each of these elements can be written as

$$\boldsymbol{x}(\xi,\eta) = \sum_{m=1}^{n_C}\sum_{n=1}^{n_C} N_m(\xi)N_n(\eta)\boldsymbol{x}\left(\xi_m,\eta_n\right)$$

$$\boldsymbol{u}(\xi,\eta) = \sum_{m=1}^{n_C}\sum_{n=1}^{n_C} N_m(\xi)N_n(\eta)\boldsymbol{u}\left(\xi_m,\eta_n\right)$$

$$\boldsymbol{t}(\xi,\eta) = \sum_{m=1}^{n_C}\sum_{n=1}^{n_C} N_m(\xi)N_n(\eta)\boldsymbol{t}\left(\xi_m,\eta_n\right) \tag{5}$$

where n_C is the number of nodes in each direction, N represents the shape functions, and ξ and η are the intrinsic coordinates of the nodes.

Lagrange polynomial-based approximation

Among the three types of spectral elements, Lobatto (Kim et al., 2008) and Gauss–Legendre elements (Muldowney & Higdon, 1995) make use of the Lagrange polynomial-based approximation. The locations of the nodes of these elements are defined by the Lobatto and the Gauss–Legendre quadrature points, respectively. The shape functions, which employ the $(n_C - 1)$th order Lagrange polynomials, are given by

$$N_m(\xi) = \prod_{l=1\ (l\neq m)}^{n_C-1} \frac{\xi - \xi_l}{\xi_m - \xi_l}$$

$$N_n(\eta) = \prod_{l=1\ (l\neq n)}^{n_C-1} \frac{\eta - \eta_l}{\eta_n - \eta_l} \tag{6}$$

where ξ_m and η_n are the coordinates of the node under consideration, and ξ_l and η_l represent the coordinates of the rest of the nodes in the same element.

Although the shape functions of Lobatto and Gauss–Legendre elements utilise the same type of interpolating polynomials, their exact expressions are different due to the disagreement in node locations. Also, it is worth mentioning that Gauss–Legendre elements are essentially discontinuous elements.

Chebyshev polynomial-based approximation

In Chebyshev elements (Dauksher & Emery, 1997), the locations of nodes in the local coordinate system are defined by

$$\xi_m = -\cos\left[\frac{\pi(m-1)}{n_C - 1}\right]$$

$$\eta_n = -\cos\left[\frac{\pi(n-1)}{n_C - 1}\right]$$

$$[m, n = 1, 2, \ldots, n_C] \tag{7}$$

The shape functions are written as

$$N_m(\xi) = \frac{2}{n_C - 1} \sum_{l=0}^{n_C-1} \frac{1}{s_m s_l} T_l(\xi_m) T_l(\xi)$$

$$N_n(\eta) = \frac{2}{n_C - 1} \sum_{l=0}^{n_C-1} \frac{1}{s_n s_l} T_l(\eta_n) T_l(\eta)$$

$$\left[s_m, s_n = \begin{cases} 1, & 1 < m, n < n_C \\ 2, & m, n = 1, n_C \end{cases},\ s_l = \begin{cases} 1, & 0 < l < n_C - 1 \\ 2, & l = 0, n_C - 1 \end{cases}\right] \tag{8}$$

where T_l represents the Chebyshev polynomials of the first kind which, in this case, are given by

$$T_l(\eta) = \cos\left(l\cos^{-1}(\eta)\right) \tag{9}$$

Discretised BIE

Once the boundary of the body has been discretised into spectral elements, the displacement BIE can be expressed in a discretised form such that

$$C_{ij}(\boldsymbol{x}')u_j(\boldsymbol{x}',s) + \sum_{l=1}^{N_e}\sum_{m=1}^{n_C}\sum_{n=1}^{n_C} P_{ij}^{lmn}(\boldsymbol{x}',s)u_j^{lmn}(\boldsymbol{x},s) = \sum_{l=1}^{N_e}\sum_{m=1}^{n_C}\sum_{n=1}^{n_C} Q_{ij}^{lmn}(\boldsymbol{x}',s)t_j^{lmn}(\boldsymbol{x},s) \tag{10}$$

where N_e is the number of spectral elements used for boundary discretisation. In Equation (10), the terms in C_{ij} can be obtained from the consideration of rigid body motion (Aliabadi, 2002, p. 51), and P_{ij}^{lmn} and Q_{ij}^{lmn}, which represent the integrals of the fundamental solutions, are given by

$$P_{ij}^{lmn}(\boldsymbol{x}',s) = \int_{-1}^{1}\int_{-1}^{1} T_{ij}[\boldsymbol{x}',\boldsymbol{x}(\xi,\eta),s]N_m(\xi)N_n(\eta)J_l(\xi,\eta)d\xi d\eta$$

$$Q_{ij}^{lmn}(\boldsymbol{x}',s) = \int_{-1}^{1}\int_{-1}^{1} U_{ij}[\boldsymbol{x}',\boldsymbol{x}(\xi,\eta),s]N_m(\xi)N_n(\eta)J_l(\xi,\eta)d\xi d\eta \tag{11}$$

where J is the Jacobian of the transformation from the global coordinate system to the intrinsic one.

Treatment of singularities

Both fundamental solutions U_{ij} and T_{ij} can be rewritten in two parts as (Dominguez, 1993)

$$U_{ij}(\boldsymbol{x}',\boldsymbol{x},s) = U_{ij}^s(\boldsymbol{x}',\boldsymbol{x}) + U_{ij}^d(\boldsymbol{x}',\boldsymbol{x},s)$$

$$T_{ij}(\boldsymbol{x}',\boldsymbol{x},s) = T_{ij}^s(\boldsymbol{x}',\boldsymbol{x}) + T_{ij}^d(\boldsymbol{x}',\boldsymbol{x},s) \tag{12}$$

where U_{ij}^s and T_{ij}^s are the fundamental solutions of three-dimensional elastostatics, and U_{ij}^d and T_{ij}^d represent dynamic contributions. In a single collocation step, if the source point is some distance away from the field element, all of the functions in Equation (12) will behave smoothly and the integrals of these functions can be evaluated directly using the standard Gauss–Legendre quadrature rule. However, if the source point happens to be one of the nodes of the field element, U_{ij}^s and T_{ij}^s will exhibit weak $O(1/r)$ and strong $O(1/r^2)$ singularity, respectively (Dominguez, 1993).

Weakly singular integrals in three-dimensional boundary element formulations can be treated directly by the transformation of variable technique (Aliabadi, Hall, & Hibbs, 1987; Lachat & Watson, 1976). The treatment of strongly singular integrals, on the other hand, makes use of both the transformation of variable technique for improving the accuracy of off-diagonal terms, and the consideration of rigid body motion for evaluating diagonal entries (Aliabadi, 2002, p. 51).

The transformation of variable technique relies on dividing a quadrilateral element into a number of triangular ones. The number of triangular elements to be divided into depends on the location of the source point, i.e. the location of singularity. Figure 2 shows the scheme for element sub-division. It is worth mentioning that for a Gauss–Legendre element, sub-divisions are always of four triangular elements since all of its nodes are interior.

Readers, who are interested in the details of the element subdivision-based transformation of variable technique as well as other methods of treating singular integrals, are recommended to consult Chapter 11 of the book by Aliabadi (2002).

Linear system of equations

Once P_{ij}^{lmn} and Q_{ij}^{lmn} have been evaluated, Equation (10) can be rewritten in a matrix form as

$$\boldsymbol{H}(s)\boldsymbol{u}(s) = \boldsymbol{G}(s)\boldsymbol{t}(s) \tag{13}$$

By separating known boundary conditions from unknown nodal values, Equation (13) can be rearranged into a linear system of equations such that

$$\boldsymbol{A}(s)\boldsymbol{x}(s) = \boldsymbol{y}(s) \tag{14}$$

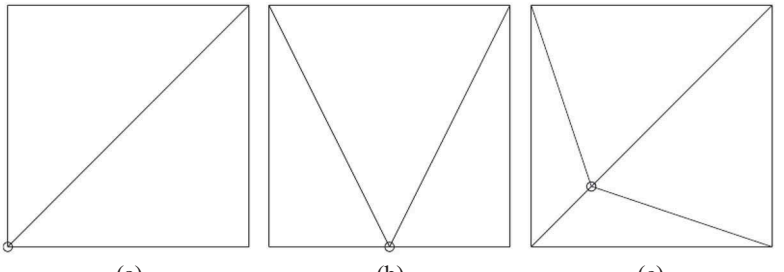

Figure 2. Scheme for element subdivision when singularity is at (a) a corner node, (b) an edge node and (c) an interior node.

Inverse Laplace transform

For an elastodynamic analysis in the Laplace domain, the displacement BIE is to be evaluated and solved for a number of Laplace terms which are given by

$$s = a + \frac{2k\pi i}{T}, \quad [k = 0, 1, 2, \ldots] \tag{15}$$

where T is the time period of interest. The response in time domain can then be obtained through Durbin's method for inverse Laplace transform (Durbin, 1974). According to Zhao (2004), Durbin's method performs the best when $a = 5/T$. Also, the number of Laplace terms to be used for an analysis depends on the *energy spectrum* of the expected response in the Laplace domain (Zou et al., 2014).

Parametric studies

Parametric studies have been conducted to examine the performances of the three types of spectral elements introduced in this paper. Benchmark results were obtained using the conventional 8-node serendipity elements. In addition to mesh convergence, convergence of numerical integration had also been found to be critical to the BEM (Rigby, 1995). In this work, the 16-, the 25- and the 36-node configurations of the three types of spectral elements have been investigated.

The parametric studies were performed using the specimen shown in Figure 3. The specimen is fixed in z-direction at its bottom surface, and is subjected to a uniform sinusoidal traction, with a frequency of 100 kHz

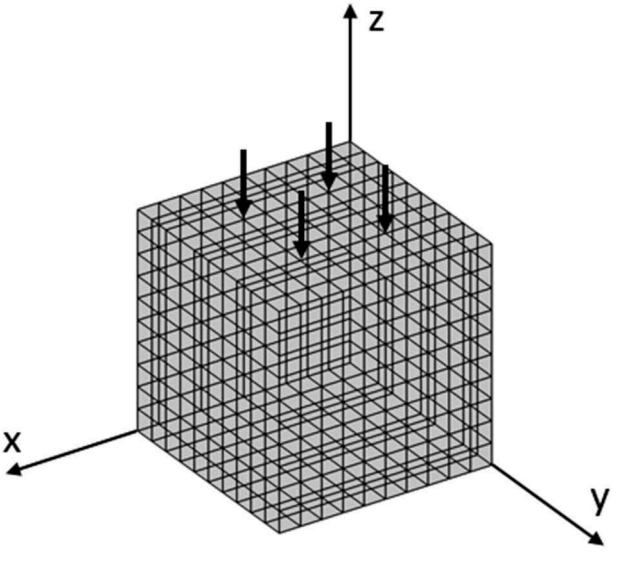

Figure 3. Schematic diagram of the specimen for the parametric studies.

and an amplitude of 1 GPa, in z-direction at its top surface. The specimen has a density of 2700 kg/m^3, a Young's modulus of 70 GPa and a Poisson's ratio of 0. For simplicity in the presentation of results, the lengths of the specimen in all three dimensions are chosen to be two wavelengths of the longitudinal wave mode, i.e. $2\lambda_L$ (λ_L = 0.0509175 m).

Figure 4 shows the Laplace domain *energy spectrum* of the above-mentioned sinusoidal traction when the time period of interest is 10^{-4} s. The response of a structure that is subjected to such a traction will contain the same frequency components. In order to arrive at a considerably accurate solution in time domain, the number of Laplace terms to be used for carrying out an analysis in the Laplace domain needs to be able to include a sufficient amount of *Laplace energy* (Zou et al., 2014). According to Figure 4, a minimum of 21 Laplace terms are required for the current example. The Laplace terms are, therefore, given by

$$s = \frac{5 + 2k\pi i}{10^{-4}}, \quad [k = 0, 1, 2, \ldots, 20] \tag{16}$$

Convergence study on numerical integration

Rigby (1995) presented a thorough investigation of the convergence of numerical integration for the three-dimensional elastostatic formulation. He concluded that for regular integrals, the numbers of integration points required for achieving convergence are solely dependent on the aspect ratios of elements, and for singular integrals that are treated by the transformation of

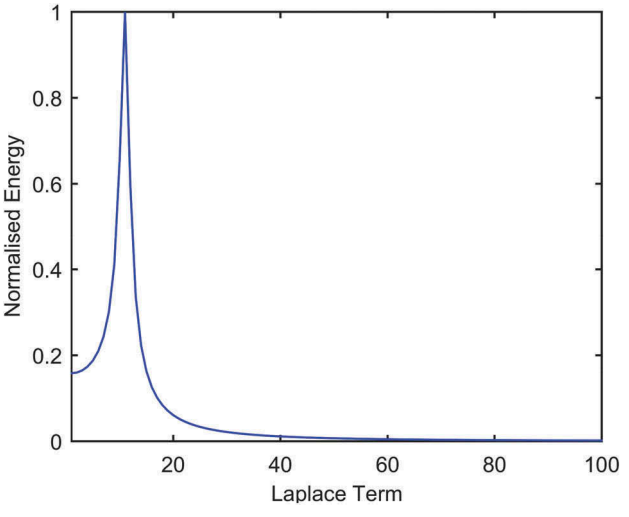

Figure 4. Laplace domain *energy spectrum* of the sinusoidal traction with a frequency of 100 kHz and an amplitude of 1 GPa.

variable technique, the angles within sub-divided triangular elements also play an important role.

In this work, the convergence of numerical integration for the dynamic functions U_{ij}^{d} and T_{ij}^{d} has been examined. It was found that the convergence is solely related to element sizes. This is due to the fact that the dynamic functions are highly oscillatory, and therefore elements of different sizes will capture different numbers of oscillation periods. Since the oscillation frequencies of the dynamic functions increase with the imaginary parts of Laplace term, it is always the Laplace term with the largest imaginary part that is to be considered in a convergence study on numerical integration. In the current example, this refers to the Laplace terms with $k = 20$.

The convergences of the values of the following integrals are assessed.

$$P_{ij}^{lmn^{s}} = \int_{-1}^{1}\int_{-1}^{1} T_{ij}^{s}[\boldsymbol{x}', \boldsymbol{x}(\xi,\eta), s]N_m(\xi)N_n(\eta)J_l(\xi,\eta)d\xi d\eta$$

$$Q_{ij}^{lmn^{s}} = \int_{-1}^{1}\int_{-1}^{1} U_{ij}^{s}[\boldsymbol{x}', \boldsymbol{x}(\xi,\eta), s]N_m(\xi)N_n(\eta)J_l(\xi,\eta)d\xi d\eta$$

$$P_{ij}^{lmn^{d}} = \int_{-1}^{1}\int_{-1}^{1} T_{ij}^{d}[\boldsymbol{x}', \boldsymbol{x}(\xi,\eta), s]N_m(\xi)N_n(\eta)J_l(\xi,\eta)d\xi d\eta$$

$$Q_{ij}^{lmn^{d}} = \int_{-1}^{1}\int_{-1}^{1} U_{ij}^{d}[\boldsymbol{x}', \boldsymbol{x}(\xi,\eta), s]N_m(\xi)N_n(\eta)J_l(\xi,\eta)d\xi d\eta \tag{17}$$

Since T_{ij}^{s} and U_{ij}^{s} contain singularities, both the regular and the singular forms of $P_{ij}^{lmn}s$ and $Q_{ij}^{lmn^{s}}$ need to be considered. The general criterion for determining the convergences of these integrals is given by (Rigby, 1995)

$$\log_{10}\left[\frac{\max\left(|I_i - I_{i-1}|\right)}{\max\left(|I_{i-1}|\right)}\right] \leq -5 \tag{18}$$

where I can be either one of the integrals in Equation (17), and the use of the subscripts i and $i-1$ indicates that the convergence studies are done in iterations, in which the numbers of integration points are incremented.

When a singular integral is treated by the transformation of variable technique, the location of singularity determines the number of triangular elements to be divided into, the angles within these sub-divided elements, and the number of integration points required for achieving convergence. In Figure 5, the nodes in each of the element configurations that are under investigation (when the aspect ratio of the element is 1:1) are separated into groups based on their relative positions. For the sake of computational efficiency, the number of integration points required for achieving

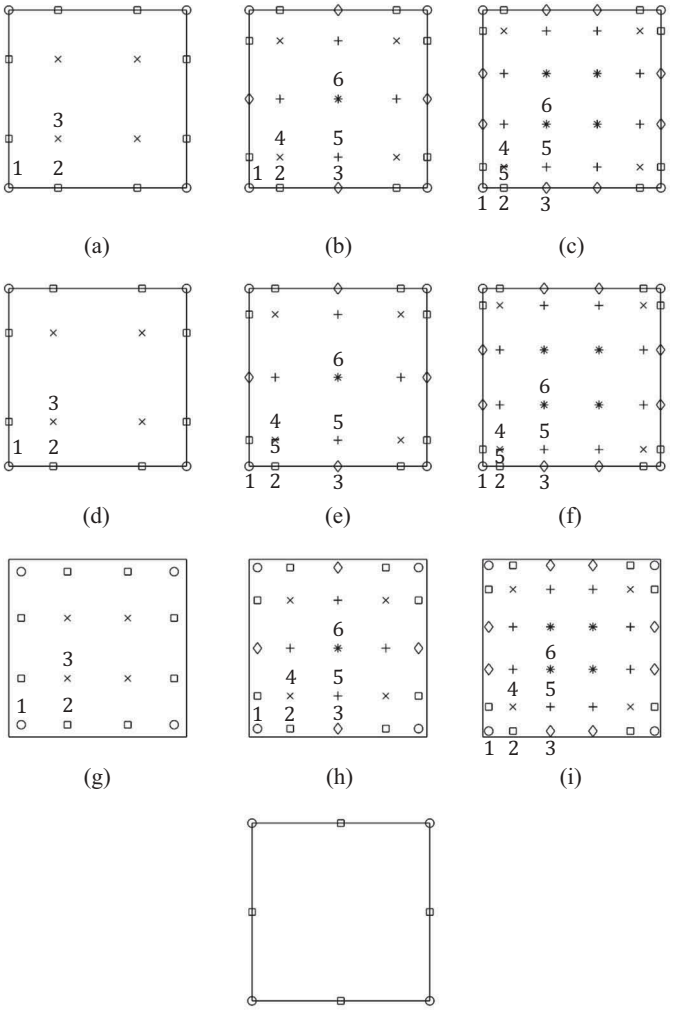

Figure 5. Grouping of the nodes within (a) 16-node, (b) 25-node and (c) 36-node Lobatto elements; (d) 16-node, (e) 25-node and (f) 36-node Chebyshev elements; (g) 16-node, (h) 25-node and (i) 36-node Gauss–Legendre elements; and (j) 8-node serendipity elements.

convergence, when each of these groups of nodes act as the locations of singularity, is to be found.

Mesh convergence study

Numerical methods such as the FEM and the BEM rely on the use of discretised sub-domains for the approximation of variables. The accuracy of approximation is highly dependent on the sizes of the elements used for discretisation. For the current example, the solution of interest is the z-direction displacement of the top surface of the specimen at where the sinusoidal traction is applied.

Although the solutions in time domain are the meaningful ones, the mesh convergence studies are to be carried out on the solutions in the Laplace domain in order to restrict the type of errors to only the spatial one. Since the oscillation frequencies of the solutions also increase with the imaginary parts of Laplace terms, the mesh convergence studies in the current example should equally make use of the Laplace term with $k = 20$.

In the next section, the results of the mesh convergence studies and of the convergence studies on numerical integration will be presented together. For elastodynamic analysis by the BEM, the results of these two sets of convergence studies are interrelated since they are both influenced by element sizes.

The responses of the structure in the current example can be solved analytically by (Eringen & Suhubi, 2013)

$$u(x,t) = \frac{1}{\rho c_1}\sum_{n=1}^{\infty}(-1)^{n-1}\left[H\left(t-\frac{(2n-1)L-x}{c_1}\right)\int_0^{t-\frac{(2n-1)L-x}{c_1}} p(\tau)d\tau - H\left(t-\frac{(2n-1)L+x}{c_1}\right)\int_0^{t-\frac{2(n-1)L+x}{c_1}} p(\tau)d\tau\right] \tag{19}$$

where p is the applied traction, ρ is the density of the material and L is the length of the structure in the direction of loading. The mesh convergence of the Laplace domain solution of the BEM is assessed by the Laplace transform of Equation (19) with the Laplace term with $k = 20$.

Results

Convergence studies

The detailed results of the convergence studies on numerical integration are given in Appendix B. The numbers of integration points required by the integrals of the static fundamental solutions do not change with element sizes. On the other hand, as an element becomes smaller, it captures less oscillations periods of the dynamic functions, and therefore less integration points are required by the respective integrals.

As shown in Figure 6, when a singular integral is treated by the transformation of variable technique, if the location of singularity is too close to an edge of an element, the angles formed at the location of singularity in some of the sub-divided elements will be highly obtuse. In a Gauss–Legendre element, when the singularity is located at Node Group 1, 2 or 3 (detailed in Figure 5), a significantly large number of integration

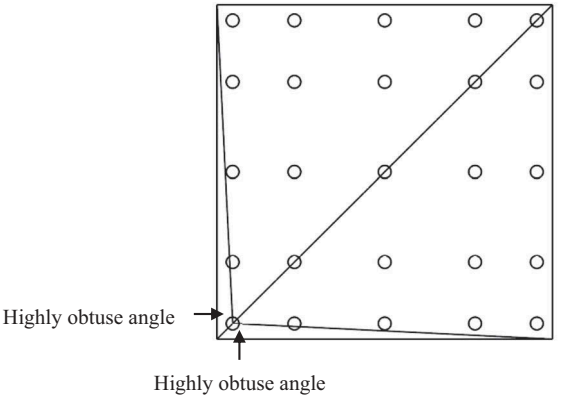

Figure 6. An example showing the highly obtuse angles formed at the point of singularity as a result of element sub-division.

points are needed. This is because these nodes are not on, but are extremely close to, the edges of the element.

It is possible to avoid the formation of highly obtuse angles by sub-dividing a quadrilateral element into more than four triangular ones (say eight). However, it is unknown whether a noteworthy reduction in total numbers of integration points will be achieved since more sub-divided elements would need to be considered. Nevertheless, it will be shown in this paper than even without further element sub-division, the use of spectral elements has already managed to achieve a computational efficiency that is substantially higher than that of the conventional BEM.

For each of the element configurations that are under investigation, the converged element size is given in Table 1. The numbers of integration points required for achieving convergence by both the regular and the singular integrals can be found in Appendix B.

In Figures 7 and 8, the mesh convergences the 16-, the 25- and the 36-node configurations of the three types of spectral elements are compared among themselves and with that of the 8-node serendipity elements. Convergences are assessed by the differences between the complex moduli

Table 1. Converged element sizes.

	Element size (λ_L = 0.0509175 m)
16-Node Lobatto	$\lambda_L/5 \times \lambda_L/5$
25-Node Lobatto	$2\lambda_L/7 \times 2\lambda_L/7$
36-Node Lobatto	$2\lambda_L/5 \times 2\lambda_L/5$
16-Node Gauss–Legendre	$\lambda_L/4 \times \lambda_L/4$
25-Node Gauss–Legendre	$\lambda_L/3 \times \lambda_L/3$
36-Node Gauss–Legendre	$\lambda_L/2 \times \lambda_L/2$
16-Node Chebyshev	$\lambda_L/5 \times \lambda_L/5$
25-Node Chebyshev	$2\lambda_L/7 \times 2\lambda_L/7$
36-Node Chebyshev	$2\lambda_L/5 \times 2\lambda_L/5$
8-Node serendipity	$2\lambda_L/19 \times 2\lambda_L/19$

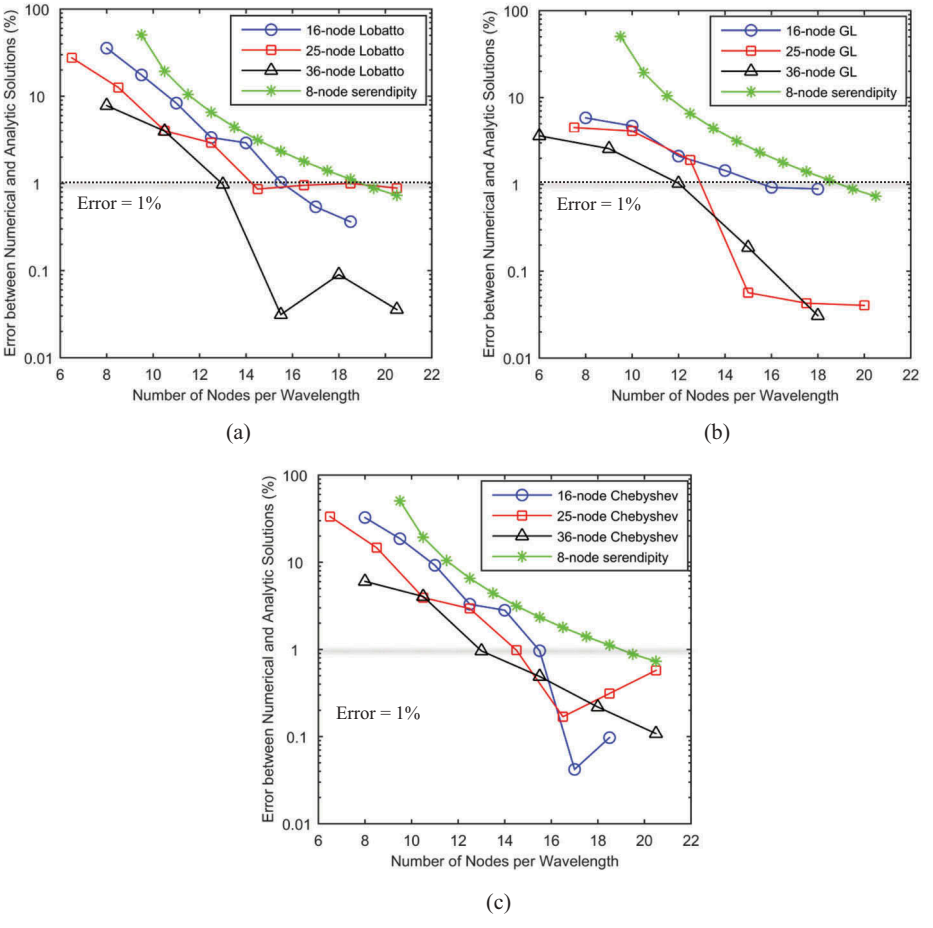

Figure 7. Comparisons, by node configuration, of the mesh convergences of (a) Lobatto, (b) Gauss–Legendre and (c) Chebyshev elements.

of the numerical and the analytic solutions. The length of the specimen is normalised by the wavelength of the longitudinal wave mode.

The comparisons of the computational expenses, shown in Table 2, are based on setting the convergence criterion of a difference of 1% between the numerical and the analytic solutions – an acceptable level of accuracy from an engineering perspective, and on computing 21 Laplace terms. The in-house source code for each type of element was written in the same structure and logic flow. The CPU times of the simulations with the spectral elements are normalised by that of the simulation with the 8-node serendipity elements. Normalised CPU times are shown here since the absolute time needed for an analysis is highly dependent on the processor used. Also, normalised values provide more direct visualisation of the savings achieved.

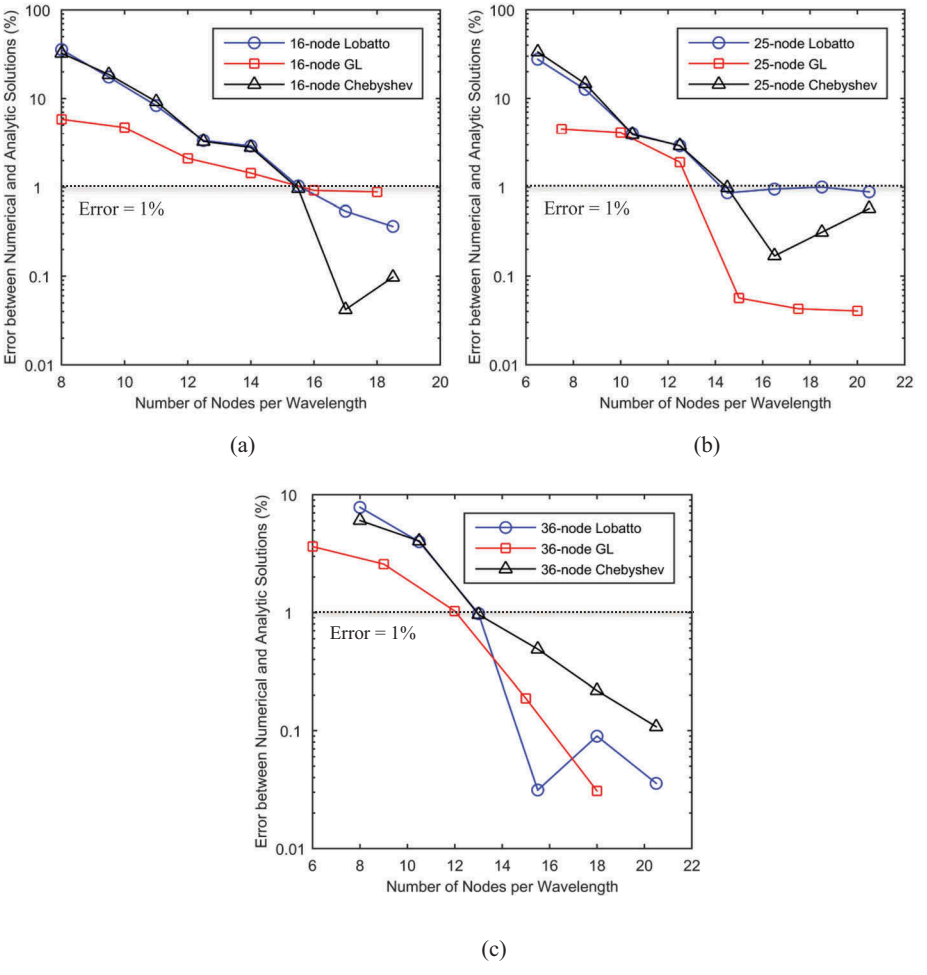

Figure 8. Comparisons, by type, of the mesh convergences of (a) 16-node, (b) 25-node and (c) 36-node spectral element configurations.

Table 2. Computational expenses of the spectral elements at convergence.

	Number of nodes per wavelength	Total number of nodes	Normalised CPU time	Improvement in CPU time (%)
16-Node Lobatto	15.5	5402	0.728	27.2
25-Node Lobatto	14.5	4706	0.496	50.4
36-Node Lobatto	13	3752	0.309	69.1
16-Node Chebyshev	15.5	5402	0.729	27.1
25-Node Chebyshev	14.5	4706	0.500	50.0
36-Node Chebyshev	13	3752	0.314	68.6
16-Node Gauss–Legendre	16	6144	0.544	45.6
25-Node Gauss–Legendre	15	5400	0.442	55.8
36-Node Gauss–Legendre	12	3456	0.275	72.5
8-Node serendipity	19	6500	1	N/A

Generally speaking, both the spectral and the 8-node serendipity elements are able to reach the same level of accuracy at convergence. However, the spectral elements achieve mesh convergence much earlier.

As shown in Table 2, the improvement in computational efficiency, brought forward by the use of spectral elements, is significant.

As illustrated in Figure 7, a general tendency that is observed for all three types of spectral elements is that when the number of nodes in an element increases, mesh convergence comes by earlier and computational expense becomes smaller. This is in contrast to the behaviours of conventional high-order elements with equally spaced nodes. The computation with those elements tends to become unstable when the number of nodes in an element reaches a certain level (Gottlieb & Orszag, 1977).

Among the three types of spectral elements considered, the mesh convergence trends of Lobatto and Chebyshev elements are very similar, and convergences are reached at the same numbers of nodes per element. Also, the CPU times required by the simulations with these elements are highly identical. When the number of nodes per element is 16 or 25, the simulation with Gauss–Legendre elements demands the largest number of nodes (i.e. more memory space) but the shortest CPU time. When the number of nodes in an element reaches 36, the use of Gauss–Legendre elements becomes the most efficient choice.

Furthermore, it is worth mentioning that the mesh convergence of the 36-node Lobatto elements is on par with the finding by Kim et al. (2008) who employed these elements in the SEM. Although the simulations in their work were conducted in time domain, the frequency of the dynamic loading and the time period of interest, which dictate mesh convergence, are the same as those in the current example. The agreement in mesh convergence trends suggests that when spectral elements are incorporated in the BEM, the amount of improvement in computational efficiency that they ought to bring can also be well realised. Since the BEM does not require domain discretisation, the current formulation is meant to use even less memory space than the SEM.

Time-domain responses

In Figure 9, the time-domain displacements of the top surface of the specimen, computed by the BEM using all of the spectral element configurations and the 8-node serendipity elements, are compared to the analytic solution. Generally speaking, the numerical and the analytic solutions are in exceptional agreement. The divergence exhibited by the numerical solutions towards the end of the time domain is due to the known limitation of Durbin's method for inverse Laplace transform (Durbin, 1974).

The scalability of the current formulation to large structures has also been testified. For determining the numbers of elements to be used for meshing the boundaries of structures, the rules set out in Table 3 were followed. The specimens considered have different lengths in the direction of loading (i.e. the z-direction) but the same cross-sectional area of $2\lambda_L \times 2\lambda_L$. The applied

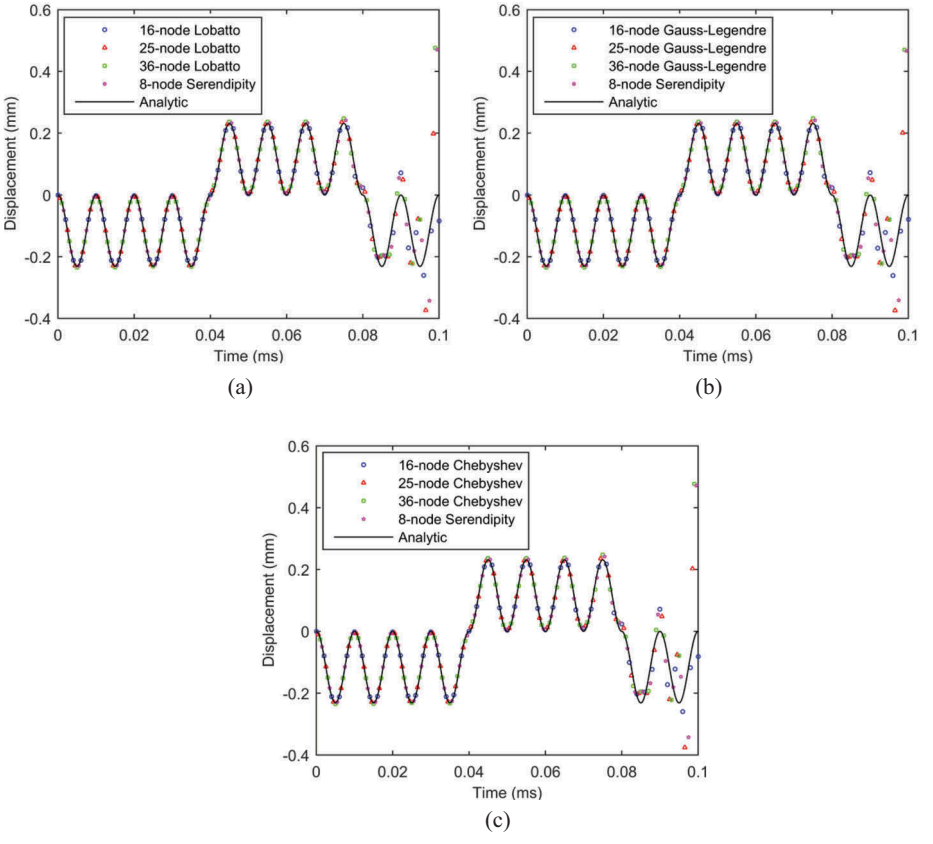

Figure 9. Comparison of the analytic solution and the displacements computed by the BSEM using (a) Lobatto, (b) Gauss–Legendre and (c) Chebyshev elements.

Table 3. Numbers of elements required for meshing two wavelengths of the longitudinal wave mode (the frequency of the applied traction is 100 kHz and the time period of interest is 0.0001 s).

	Number of elements for $2\lambda_L$
8-Node serendipity	19
16-Node Lobatto	10
25-Node Lobatto	7
36-Node Lobatto	5
16-Node Gauss–Legendre	8
25-Node Gauss–Legendre	6
36-Node Gauss–Legendre	4
16-Node Chebyshev	10
25-Node Chebyshev	7
36-Node Chebyshev	5

traction and the time period of interest are the same as those in the previous example.

Through numerical simulations, it was observed that the percentage saving in total number of nodes and CPU times, shown in Table 2, does not change with the lengths of structures. This suggests that spectral

elements are truly appropriate for the dynamic analysis of large engineering structures since the absolute amount of saving in computational expenses increases with the sizes of structures. Also, when computational resources are limited such that fully converged meshes cannot be afforded, simulations with spectral elements will result in more accurate solutions.

Numerical experiments

In this section, the performance of the BSEM will be further assessed by numerical experiments. In order to achieve a balance between computational efficiency and convenient numerical integration, 36-node Lobatto elements were chosen to be used. Although 36-node Gauss–Legendre elements require less computational resources, they are more difficult to implement due the extremely large numbers of integration points needed for evaluating singular integrals.

High-frequency applications

Two cubic specimens, which measure $3\lambda_L \times 3\lambda_L \times 3\lambda_L$ ($\lambda_L = 0.0169725$ m) and $4\lambda_L \times 4\lambda_L \times 4\lambda_L$ ($\lambda_L = 0.0101835$ m), were considered in the first numerical experiment. The material properties of the specimens are the same as those of the specimen used for the parametric studies. Both specimens are fixed in the z-direction at their bottom surfaces and are subjected to a sinusoidal traction with a peak amplitude of 1 GPa in the z-direction at their top surfaces. The excitation frequencies are 300 and 500 kHz, respectively. For either specimen, 21 Laplace terms are needed for the simulation. The time periods of interest in the simulations are 3.33×10^{-5} s and 2×10^{-5} s.

For both specimens, the comparisons of the mesh convergences of the 36-node Lobatto elements and the 8-node serendipity elements are shown in Figure 10. The comparisons of the computational expenses of the simulations with these elements are displayed in Table 4. As expected, the spectral elements reach mesh convergence much more quickly. Also, the fact that the numbers of nodes required per wavelength for achieving convergence are very similar to those determined by the parametric studies acts as a solid proof of the consistency of the BSEM.

A three-dimensional specimen

In the second numerical experiment, the capability of the BSEM in modelling structures with realistic material properties will be examined. While the Young's modulus and the density of the specimen remain 2700 kg/m^3 and 70 GPa, the Poisson's ratio is now 0.33. The specimen, shown in Figure 11, is subjected to the same applied load and boundary condition as Specimen 2 in

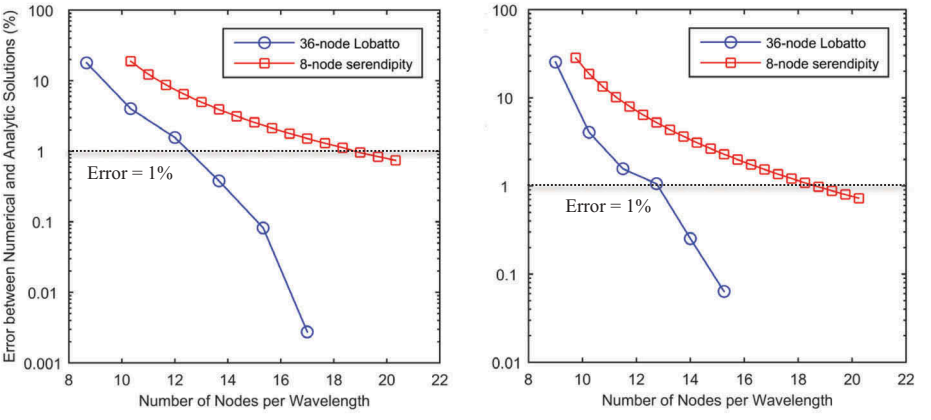

Figure 10. Mesh convergences of the 36-node Lobatto elements and the 8-node serendipity elements for the analysis of (a) Specimen 1 ($3\lambda_L \times 3\lambda_L \times 3\lambda_L$, 300 kHz) and (b) Specimen 2 ($4\lambda_L \times 4\lambda_L \times 4\lambda_L$, 500 kHz).

Table 4. Computational expenses of the analysis of (a) Specimen 1 and (b) Specimen 2.

	Number of nodes per wavelength	Total number of nodes	Normalised CPU time	Improvement in CPU time (%)
36-Node Lobatto	14	9062	0.439	56.1
8-Node serendipity	19	14,114	1	N/A

(a)

	Number of Nodes per Wavelength	Total Number of Nodes	Normalised CPU Time	Improvement in CPU Time (%)
36-Node Lobatto	13	15,002	0.353	64.7
8-Node serendipity	19	24,644	1	N/A

(b)

the previous experiment was. It has a dimension of 0.02 m × 0.01 m × 0.01 m ($\sim 2\lambda_L \times \lambda_L \times \lambda_L$) and is discretised into 3, 3 and 6 elements of 0.00333 m × 0.00333 m in its x-, y- and z-direction. This is equivalent to meshing each wavelength of the longitudinal wave mode by 19 nodes – a number that is much higher than what is required for achieving convergence as determined by the parametric studies. In the simulation, the time period of interest is 2×10^{-5} s, and a total of 21 Laplace terms were considered.

In this experiment, the solutions of interest are the lateral and the longitudinal displacement of the corner of the top surface of the specimen. Since there is no analytic solution available for such a problem, the solutions of the BSEM were validated by those of the FEM obtained using Abaqus®/Explicit.

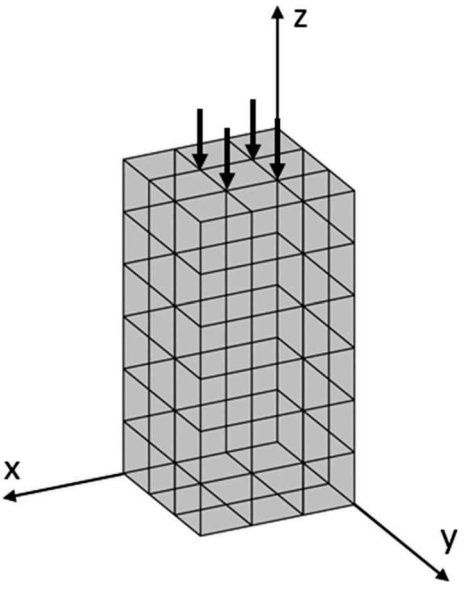

Figure 11. Schematic diagram and boundary element mesh of the specimen used in the second numerical experiment.

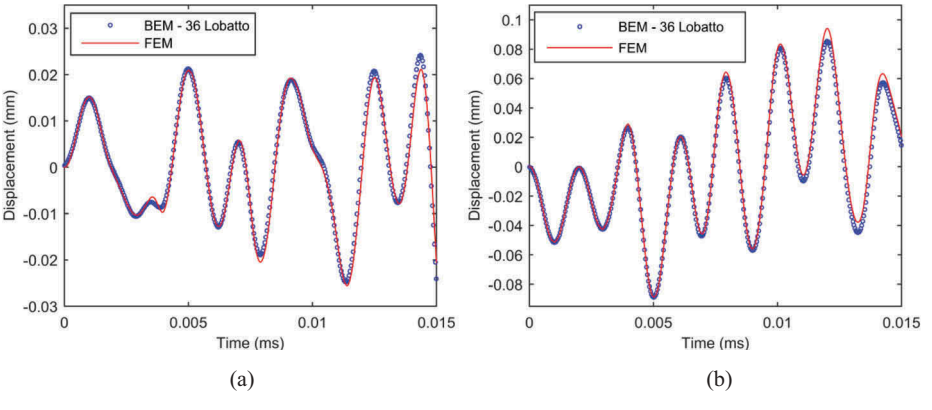

Figure 12. (a) Lateral and (b) horizontal displacements of the corner of the top surface of the specimen computed by the BSEM and the FEM.

In Figure 12, the comparisons of the results of the FEM and of the BSEM with 36-node Lobatto elements are presented. The phases of the responses are highly identical and the maximum difference between the amplitudes is within 5%. Based on the reasonably high level of agreement, it can be concluded that the BSEM formulated in this work is a valid numerical tool for the analysis of three-dimensional elastic structures that are subjected to high-frequency dynamic loadings.

The total numbers of nodes required for achieving convergence by the BSEM with 36-node Lobatto elements and by the FEM with 8-node linear

solid elements and explicit integration scheme are 2252 and 262,701, respectively. Although this comparison is between two different types of elements, it illustrates the amount of saving in computational costs that the BSEM has managed to achieve over a widely used commercial FEM package.

Also, it is worth mentioning that the BSEM has been experimentally validated through modelling the piezoelectric smart structures that are commonly used in damage detection applications (Zou & Aliabadi, 2017).

Conclusion

In this paper, an efficient and accurate numerical method for modelling high-frequency wave propagation in three-dimensional engineering structures has been presented. By employing high-order spectral elements for boundary discretisation, a significant reduction in the demand on computational resources has been achieved by the BSEM over the conventional BEM. A systematic study on the implementation of spectral elements in the BEM has been demonstrated. Due to the nature of BIEs, the implementation is not exactly straightforward.

Three types of spectral elements – Lobatto, Gauss–Legendre and Chebyshev elements – with three different node configurations have been considered. Among these, 36-node Lobatto elements provide the optimal balance between convenient implementation and efficient computation. Using these elements, numerical experiments have been conducted in order to assess the capabilities of the BSEM in modelling high-frequency applications and realistic engineering structures. The BSEM has also been validated against a well-established FEM.

Disclosure statement

No potential conflict of interest was reported by the authors.

ORCID

Fangxin Zou http://orcid.org/0000-0001-5416-9176

References

Aliabadi, M. H. (2002). *The boundary element method. Volume 2, applications in solids and structures*. Wiley: United Kingdom.

Aliabadi, M. H., Hall, W. S., & Hibbs, T. T. (1987). Exact singularity cancelling for the potential kernel in the boundary element method. *Communications in Applied Numerical Methods*, *3*(2), 123–128.

Benedetti, I., Aliabadi, M., & Davi, G. (2008). A fast 3D dual boundary element method based on hierarchical matrices. *International Journal of Solids and Structures*, *45*(7), 2355–2376.

Benedetti, I., & Aliabadi, M. H. (2010). A fast hierarchical dual boundary element method for three-dimensional elastodynamic crack problems. *International Journal for Numerical Methods in Engineering*, *84*(9), 1038–1067.

Dauksher, W., & Emery, A. F. (1997). Accuracy in modeling the acoustic wave equation with Chebyshev spectral finite elements. *Finite Elements in Analysis and Design*, *26*(2), 115–128.

Dominguez, J. (1993). *Boundary elements in dynamics: Wit Press*. https://www.witpress.com/books/978-1-85312-258-3

Durbin, F. (1974). Numerical inversion of Laplace transforms: An efficient improvement to Dubner and Abate's method. *The Computer Journal*, *17*(4), 371–376.

Eringen, A. C., & Suhubi, E. S. (2013). *Linear theory: Academic press*. https://www.elsevier.com/books/linear-theory/eringen/978-0-12-240602-7

Giurgiutiu, V. (2005). Tuned lamb wave excitation and detection with piezoelectric wafer active sensors for structural health monitoring. *Journal of Intelligent Material Systems and Structures*, *16*(4), 291–305.

Gottlieb, D., & Orszag, S. A. (1977). *Numerical analysis of spectral methods: Theory and applications* (Vol. 26). Siam. https://epubs.siam.org/doi/book/10.1137/1.9781611970425

Gottlieb, D., & Orszag, S. A. (1983). *Numerical analysis of spectral methods: Theory and applications: Society for industrial and applied mathematics*. https://epubs.siam.org/doi/book/10.1137/1.9781611970425

Ha, S., & Chang, F.-K. (2010). Optimizing a spectral element for modeling PZT-induced lamb wave propagation in thin plates. *Smart Materials and Structures*, *19*(1), 015015.

Haywood, J., Coverley, P., Staszewski, W. J., & Worden, K. (2004). An automatic impact monitor for a composite panel employing smart sensor technology. *Smart Materials and Structures*, *14*(1), 265.

Ihn, J.-B., & Chang, F.-K. (2004). Detection and monitoring of hidden fatigue crack growth using a built-in piezoelectric sensor/actuator network: I. diagnostics. *Smart Materials and Structures*, *13*(3), 609.

Kim, Y., Ha, S., & Chang, F.-K. (2008). Time-domain spectral element method for built-in piezoelectric-actuator-induced lamb wave propagation analysis. *AIAA Journal*, *46*(3), 591–600.

Komatitsch, D., Barnes, C., & Tromp, J. (2000). Simulation of anisotropic wave propagation based upon a spectral element method. *Geophysics*, *65*(4), 1251–1260.

Komatitsch, D., & Tromp, J. (1999). Introduction to the spectral element method for three-dimensional seismic wave propagation. *Geophysical Journal International*, *139*(3), 806–822.

Komatitsch, D., & Tromp, J. (2002). Spectral-element simulations of global seismic wave propagation—I. Validation. *Geophysical Journal International*, *149*(2), 390–412.

Komatitsch, D., & Vilotte, J.-P. (1998). The spectral element method: An efficient tool to simulate the seismic response of 2D and 3D geological structures. *Bulletin of the Seismological Society of America*, *88*(2), 368–392.

Lachat, J., & Watson, J. (1976). Effective numerical treatment of boundary integral equations: A formulation for three-dimensional elastostatics. *International Journal for Numerical Methods in Engineering*, *10*(5), 991–1005.

Mallardo, V., & Aliabadi, M. (2012). An adaptive fast multipole approach to 2D wave propagation. *Computer Modeling in Engineering and Sciences*, *87*(2), 77.

Mallardo, V., Aliabadi, M., & Khodaei, Z. S. (2013). Optimal sensor positioning for impact localization in smart composite panels. *Journal of Intelligent Material Systems and Structures*, *24*(5), 559–573.

Mallardo, V., Sharif Khodaei, Z., & Aliabadi, F. M. (2016). A Bayesian approach for sensor optimisation in impact identification. *Materials*, *9*(11), 946.

Muldowney, G., & Higdon, J. (1995). A spectral boundary element approach to three-dimensional Stokes flow. *Journal of Fluid Mechanics*, *298*, 167–192.

Occhialini, J., Muldowney, G., & Higdon, J. (1992). Boundary integral/spectral element approaches to the Navier–Stokes equations. *International Journal for Numerical Methods in Fluids*, *15*(12), 1361–1381.

Patera, A. T. (1984). A spectral element method for fluid dynamics: Laminar flow in a channel expansion. *Journal of Computational Physics*, *54*(3), 468–488.

Peng, H., Meng, G., & Li, F. (2009). Modeling of wave propagation in plate structures using three-dimensional spectral element method for damage detection. *Journal of Sound and Vibration*, *320*(4), 942–954.

Rigby, R. (1995). *Boundary element analysis of cracks in aerospace structures*. PhD Thesis, Wessex Institute of Technology, University of Portsmouth.[Links].

Sharif-Khodaei, Z., & Aliabadi, M. H. (2014). Assessment of delay-and-sum algorithms for damage detection in aluminium and composite plates. *Smart Materials and Structures*, *23*(7), 075007.

Shen, L., & Liu, Y. (2007). An adaptive fast multipole boundary element method for three-dimensional acoustic wave problems based on the Burton–Miller formulation. *Computational Mechanics*, *40*(3), 461–472.

Wen, P. H., Aliabadi, M. H., & Rooke, D. P. (1998). Cracks in three dimensions: A dynamic dual boundary element analysis. *Computer Methods in Applied Mechanics and Engineering*, *167*(1), 139–151.

Worden, K., & Staszewski, W. (2000). Impact location and quantification on a composite panel using neural networks and a genetic algorithm. *Strain*, *36*(2), 61–68.

Żak, A. (2009). A novel formulation of a spectral plate element for wave propagation in isotropic structures. *Finite Elements in Analysis and Design*, *45*(10), 650–658.

Zhao, X. (2004). An efficient approach for the numerical inversion of Laplace transform and its application in dynamic fracture analysis of a piezoelectric laminate. *International Journal of Solids and Structures*, *41*(13), 3653–3674.

Zienkiewicz, O. C., & Taylor, R. L. (2000). *The finite element method: Solid mechanics* (Vol. 2). Butterworth-heinemann. https://www.amazon.com/Finite-Element-Method-Solid-Mechanics/dp/0470395052

Zou, F., & Aliabadi, M. (2017). On modelling three-dimensional piezoelectric smart structures with boundary spectral element method. *Smart Materials and Structures*, *26*(5), 055015.

Zou, F., & Aliabadi, M. H. (2015). A boundary element method for detection of damages and self-diagnosis of transducers using electro-mechanical impedance. *Smart Materials and Structures, 24*, 9.

Zou, F., Benedetti, I., & Aliabadi, M. H. (2014). A boundary element model for structural health monitoring using piezoelectric transducers. *Smart Materials and Structures*, *23*(1), 015022.

Appendix A

The fundamental solutions in Equation (3) are given by Wen et al. (1998)

$$U_{ij}(\boldsymbol{x}', \boldsymbol{x}, s) = \frac{1}{4\pi G}\left(\psi\delta_{ij} - \chi r_{,i} r_{,j}\right)$$

$$T_{ij}(\boldsymbol{x}', \boldsymbol{x}, s) = \frac{1}{4\pi}\left[\left(\psi_{,r} - \frac{\chi}{r}\right)\left(\frac{\partial r}{\partial n}\delta_{ij} + r_{,j}n_i\right) - 2\frac{\chi}{r}\left(n_j r_{,i} - 2r_{,i}r_{,j}\frac{\partial r}{\partial n}\right)\right.$$
$$\left. -2\chi_{,r}r_{,i}r_{,j}\frac{\partial r}{\partial n} + \left(\frac{{c_1}^2}{{c_2}^2} - 2\right)\left(\psi_{,r} - \chi_{,r} - 2\frac{\chi}{r}\right)n_j r_{,i}\right]$$

where δ_{ij} is the Kronecker delta, $\boldsymbol{n}$ is the unit normal vector, and

$$\psi = \frac{e^{-\left(\frac{sr}{c_2}\right)}}{r} + \left(\frac{1 + \frac{sr}{c_2}}{\left(\frac{sr}{c_2}\right)^2}\right)\left(\frac{e^{-\left(\frac{sr}{c_2}\right)}}{r}\right) - \frac{{c_2}^2}{{c_1}^2}\left(\frac{1 + \frac{sr}{c_1}}{\left(\frac{sr}{c_1}\right)^2}\right)\left(\frac{e^{-\left(\frac{sr}{c_1}\right)}}{r}\right)$$

$$\chi = 3\psi - 2\frac{e^{-\left(\frac{sr}{c_2}\right)}}{r} - \frac{{c_2}^2}{{c_1}^2}\left(\frac{e^{-\left(\frac{sr}{c_1}\right)}}{r}\right)$$

$$r = |\boldsymbol{x}' - \boldsymbol{x}|$$

$$G = \frac{E}{2(1 - \nu)}$$

Appendix B

Table B1. Numbers of integration points required by the integrals of the static fundamental solutions for achieving convergence (the numbers of integration points do not change with element sizes).

	$P_{ij}^{lmn^5}, Q_{ij}^{lmn^5}$						
		Singular (location of singularity)					
	Regular	Node 1	Node 2	Node 3	Node 4	Node 5	Node 6
16-Node Lobatto	8 × 8	8 × 8	12 × 12	14 × 14	N/A	N/A	N/A
25-Node Lobatto	8 × 8	8 × 8	14 × 14	10 × 10	18 × 18	22 × 22	10 × 10
36-Node Lobatto	8 × 8	8 × 8	16 × 16	10 × 10	22 × 22	28 × 28	14 × 14
16-Node Gauss–Legendre	8 × 8	28 × 28	46 × 46	14 × 14	N/A	N/A	N/A
25-Node Gauss–Legendre	8 × 8	34 × 34	62 × 62	62 × 62	16 × 16	18 × 18	10 × 10
36-Node Gauss–Legendre	8 × 8	40 × 40	76 × 76	94 × 94	18 × 18	22 × 22	12 × 12
16-Node Chebyshev	8 × 8	8 × 8	12 × 12	16 × 16	N/A	N/A	N/A
25-Node Chebyshev	8 × 8	8 × 8	14 × 14	10 × 10	20 × 20	24 × 24	10 × 10
36-Node Chebyshev	8 × 8	8 × 8	18 × 18	10 × 10	26 × 26	34 × 34	14 × 14
8-Node serendipity	6 × 6	8 × 8	10 × 10	N/A	N/A	N/A	N/A

Table B2. Numbers of integration points required by the integrals of the dynamic functions for achieving convergence ($s = \frac{5+2\times21\times\pi i}{10^{-4}}$).

Element size (λ_L = 0.0509175 m)	16-Node Lobatto	25-Node Lobatto	36-Node Lobatto	16-Node Gauss–Legendre	25-Node Gauss–Legendre	36-Node Gauss–Legendre	16-Node Chebyshev	25-Node Chebyshev	36-Node Chebyshev	8-Node serendipity
$\lambda_L \times \lambda_L$						16 × 16				
$2\lambda_L/3 \times 2\lambda_L/3$		12 × 12	12 × 12		12 × 12	12 × 12		12 × 12	12 × 12	
$\lambda_L/2 \times \lambda_L/2$		12 × 12	12 × 12	12 × 12	12 × 12	12 × 12		12 × 12	12 × 12	
$2\lambda_L/5 \times 2\lambda_L/5$	10 × 10	10 × 10	10 × 10	10 × 10	10 × 10	12 × 12	10 × 10	10 × 10	10 × 10	10 × 10
$\lambda_L/3 \times \lambda_L/3$	10 × 10	10 × 10	10 × 10	10 × 10	10 × 10	10 × 10	10 × 10	10 × 10	10 × 10	10 × 10
$2\lambda_L/7 \times 2\lambda_L/7$	10 × 10	10 × 10	10 × 10	10 × 10	10 × 10	10 × 10	10 × 10	10 × 10	10 × 10	8 × 8
$\lambda_L/4 \times \lambda_L/4$	8 × 8	10 × 10	10 × 10	10 × 10	10 × 10		8 × 8	10 × 10	10 × 10	8 × 8
$2\lambda_L/9 \times 2\lambda_L/9$	8 × 8	10 × 10		10 × 10			8 × 8	10 × 10		8 × 8
$\lambda_L/5 \times \lambda_L/5$	8 × 8	10 × 10		10 × 10			8 × 8	10 × 10		8 × 8
$2\lambda_L/11 \times 2\lambda_L/11$	8 × 8			10 × 10			8 × 8			8 × 8
$\lambda_L/6 \times \lambda_L/6$	8 × 8			10 × 10			8 × 8			8 × 8
$2\lambda_L/13 \times 2\lambda_L/13$										8 × 8
$\lambda_L/7 \times \lambda_L/7$										8 × 8
$2\lambda_L/15 \times 2\lambda_L/15$										8 × 8
$\lambda_L/8 \times \lambda_L/8$										8 × 8
$2\lambda_L/17 \times 2\lambda_L/17$										8 × 8
$\lambda_L/9 \times \lambda_L/9$										8 × 8
$2\lambda_L/19 \times 2\lambda_L/19$										8 × 8
$\lambda_L/10 \times \lambda_L/10$										8 × 8